

OPEN

# Tuning the Electrical and Thermoelectric Properties of N Ion Implanted SrTiO<sub>3</sub> Thin Films and Their Conduction Mechanisms

Anuradha Bhogra<sup>1</sup>, Anha Masarrat<sup>1,2</sup>, Ramcharan Meena<sup>1</sup>, Dilruba Hasina<sup>3</sup>, Manju Bala<sup>4</sup>, Chung-Li Dong<sup>5</sup>, Chi-Liang Chen<sup>6</sup>, Tapobrata Som<sup>3</sup>, Ashish Kumar<sup>1</sup> & Asokan Kandasami<sup>1</sup>

The SrTiO<sub>3</sub> thin films were fabricated by pulsed laser deposition. Subsequently ion implantation with 60 keV N ions at two different fluences  $1 \times 10^{16}$  and  $5 \times 10^{16}$  ions/cm<sup>2</sup> and followed by annealing was carried out. Thin films were then characterized for electronic structure, morphology and transport properties. X-ray absorption spectroscopy reveals the local distortion of TiO<sub>6</sub> octahedra and introduction of oxygen vacancies due to N implantation. The electrical and thermoelectric properties of these films were measured as a function of temperature to understand the conduction and scattering mechanisms. It is observed that the electrical conductivity and Seebeck coefficient (*S*) of these films are significantly enhanced for higher N ion fluence. The temperature dependent electrical resistivity has been analysed in the temperature range of 80–400 K, using various conduction mechanisms and fitted with band conduction, near neighbour hopping (NNH) and variable range hopping (VRH) models. It is revealed that the band conduction mechanism dominates at high temperature regime and in low temperature regime, there is a crossover between NNH and VRH. The *S* has been analysed using the relaxation time approximation model and dispersive transport mechanism in the temperature range of 300–400 K. Due to improvement in electrical conductivity and thermopower, the power factor is enhanced to  $15 \mu\text{Wm}^{-1} \text{K}^{-2}$  at 400 K at the higher ion fluence which is in the order of ten times higher as compared to the pristine films. This study suggests that ion beam can be used as an effective technique to selectively alter the electrical transport properties of oxide thermoelectric materials.

Increasing demand for the clean energy resources led to an alternative approach of environment friendly high performance thermoelectric devices to reuse the waste heat via solid state refrigeration and power generation<sup>1</sup>. Thermoelectric (TE) devices can be used to convert a temperature difference into electricity and vice-versa. Despite their several advantages such as small size, portability and scalability etc<sup>1</sup>, their low efficiency makes it difficult to meet the basic requirement for a practical application like power generation and cooling. The thermoelectric performance is related to a dimensionless figure of merit  $ZT = S^2\sigma T/\kappa$  where, *T*, *S*,  $\sigma$  and  $\kappa$  represent absolute temperature, Seebeck coefficient, electrical conductivity and thermal conductivity, respectively. The optimization of *ZT* is challenging due to inter-related material properties like  $\sigma$ ,  $\kappa$ . Recent studies have been focussing on SnSe, Bi<sub>2</sub>Te<sub>3</sub>, skutterudites, half heusler, clathrates as thermoelectric materials and have been explored for commercial purposes<sup>2,3</sup>. However, these materials are toxic, expensive, and rare in nature which is an important concern for practical use and large scale commercialization. Due to these limitations, oxide TE materials have received renowned attention for mid- and high temperature thermoelectric applications based on their thermal and chemical stabilities in air and at high temperatures<sup>4</sup>. Among oxide TE, the layered cobalt oxides, such as Na<sub>x</sub>CoO<sub>2</sub> and Ca<sub>3</sub>Co<sub>4</sub>O<sub>9</sub> (CO-349), are known to be good *p*-type TE materials<sup>5</sup> while *n*-type oxides are relatively unavailable. The most promising candidates for *n*-type oxide TE materials include perovskite-type SrTiO<sub>3</sub> (STO) and CaMnO<sub>3</sub><sup>6</sup>.

<sup>1</sup>Inter-University Accelerator Centre, Aruna Asaf Ali Marg, New Delhi, 110067, India. <sup>2</sup>Department of Physics, Jamia Milia Islamia University, New Delhi, 110025, India. <sup>3</sup>Institute of Physics, Bhubaneswar, 751005, India. <sup>4</sup>Department of Physics and Astrophysics, Delhi University, New Delhi, 110016, India. <sup>5</sup>Research Center for X-ray Science, Department of Physics, Tamkang University, Tamsui, 251, Taiwan. <sup>6</sup>National Synchrotron Radiation Research Centre, Hsinchu, Taiwan. Correspondence and requests for materials should be addressed to A.B. (email: [anu.bhogra@gmail.com](mailto:anu.bhogra@gmail.com)) or A.K. (email: [asokaniyac@gmail.com](mailto:asokaniyac@gmail.com))

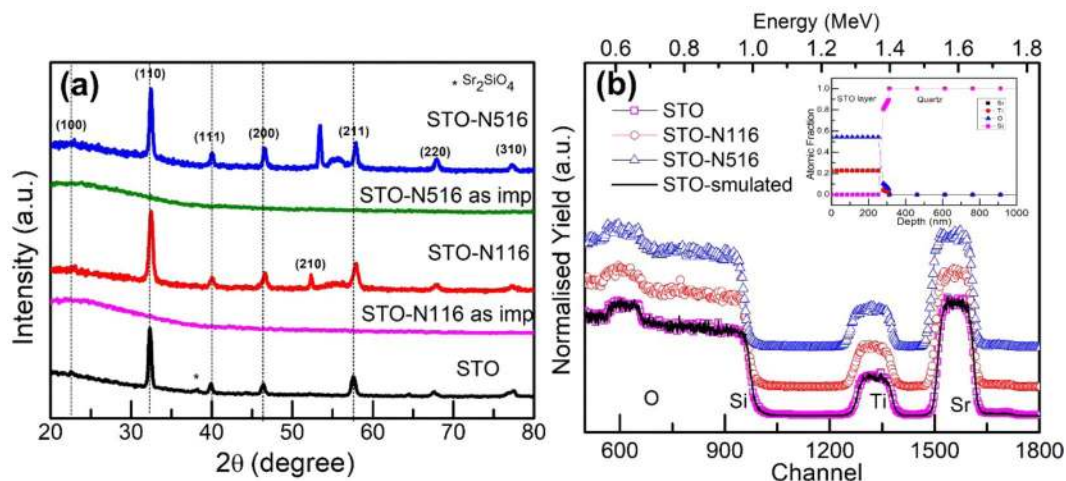


**Figure 1.** (a) X-ray diffraction patterns of STO thin films: STO, STO-N116 and STO-N516. The as-implanted samples for ion fluences  $1 \times 10^{16}$  and  $5 \times 10^{16}$  ion/cm<sup>2</sup> show amorphous nature. (b) RBS spectra of STO films: STO, STO-N116 and STO-N516. The inset shows the depth profile of STO film as determined from X-RUMP simulation.

Different physical approaches such as band engineering, nanostructuring, low dimensionality, superlattices and mechanism based strategies like resonant levels, band convergence, and spin Seebeck effect<sup>7,8</sup> so on have been adopted to improve the ZT of these materials. Ion beam technique is one of the conventional tools in semiconductors to introduce dopants and defects in a controlled way by selecting strategically suitable energies and ion doses. This technique provides independent control of dose and penetration depth. However, ion implantation has been scarcely explored in thermoelectric materials<sup>9,10</sup>. It is reported that ion beam technique can contribute in the modification of lattice thermal conductivity effectively by radiation induced defects engineering or nanostructuring<sup>11,12</sup>. Thus, this technique allows a new approach for improvement of thermoelectric efficiency and requires more studies.

In the present work, we focus on perovskite material STO which is increasingly recognised as *n*-type thermoelectric material because of its unique electronic structure and tunability<sup>13–15</sup>. It has a wide band gap of 3.2 eV and exhibits good thermoelectric properties due to heavy 3d electrons<sup>16,17</sup>. Ohta and co-authors have reported that low dimensionality in STO can greatly enhance the S as large as five times compared to the bulk system<sup>18</sup>. An extremely high ZT of ~2.4 at 300 K has been achieved for Nb doped STO thin layer attributed to a two dimensional electron gas layer (2DEG) formed resulting in quantum confinement effect<sup>19,20</sup>. In 2007, Liu *et al.* reported a reduction in resistivity of STO films due to N ion implantation<sup>21</sup>. Literature survey shows that extensive studies have been carried out on the electric and thermoelectric properties of STO<sup>13</sup>. However, there is no previous study on the effect of ion implantation induced defects on the electrical and thermoelectric properties. This study focuses on the effect of low energy N ion implantation on the crystal and electronic structures, electrical and thermoelectric properties of STO. In this work, we also attempt to determine the possible conduction mechanisms at various temperature ranges.

## Results and Discussion

All the films were deposited by pulsed laser deposition on Si substrate using STO target and implanted with 60 keV N<sup>+</sup> ions with fluence;  $1 \times 10^{16}$  and  $5 \times 10^{16}$  ions/cm<sup>2</sup>. Post implantation vacuum annealing was performed at 700 °C for 2 h. For simplicity, hereafter, annealed films of pristine,  $1 \times 10^{16}$  ions/cm<sup>2</sup> and  $5 \times 10^{16}$  ions/cm<sup>2</sup> are referred as STO, STO-N116, and STO-N516, respectively.

Figure 1(a) shows the XRD spectra of pristine and N implanted STO films. Implantation of 60 keV N<sup>+</sup> ions resulted in amorphization in the top layers of STO film as probed by XRD and hence these films were subjected to vacuum annealing of 2 hrs. After annealing, a crystalline phase evolves and gets more pronounced at higher fluence. All the STO films show an intense, sharp reflections assigned to planes of (110), (111), (200), (220) and (310) matching with the JCPDS No. 03–0769 and confirm the formation of cubic perovskite phase. However, a very small silicate phase is observed in pristine sample only. As evident from the XRD, this phase is absent after ion implantation. Hence, silicate is not expected to play a major role in the electrical properties and Seebeck coefficient of N ion implanted STO. The Rietveld refinement has been carried out to calculate the lattice parameters. The calculated lattice parameter of STO is comparable to the near stoichiometric samples about 3.905 nm<sup>22</sup>. After N implantation, the lattice parameter changes slightly and remains almost the same for both the STO-N116 and STO-N516. No significant change is observed since the concentration is very low. The bond length of pristine sample calculated from the Rietveld analysis is found to be in accordance with the literature<sup>23</sup>. It is observed that the bond lengths Ti–O in TiO<sub>6</sub> octahedra are almost constant after implantation (see Supplementary Information). A small shift in all the diffracted peaks is observed due to the presence of lattice strain arising from the ion implantation. Figure 1(b) shows the experimental RBS spectra of STO-P, STO-N116 and STO-N516 along with the simulated spectrum of STO-P using XRUMP Software<sup>24</sup>. The average thickness is estimated to be 280 nm which is close to the measured value. The inset in Fig. 1(b) shows the atomic fraction of

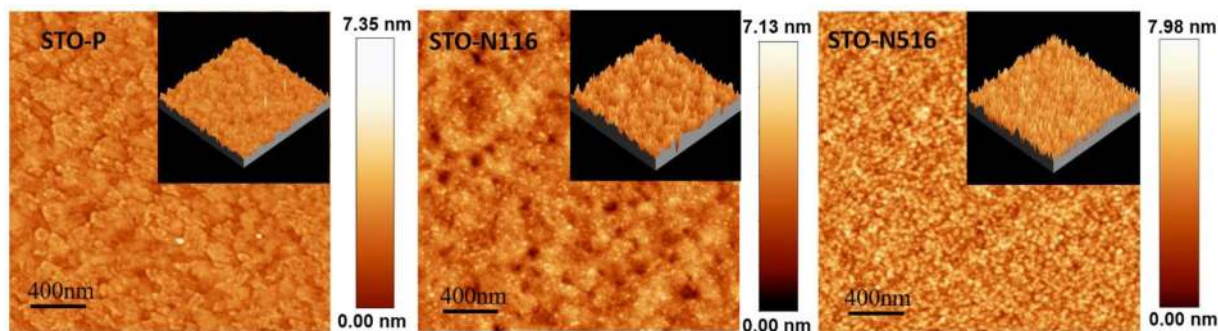


**Figure 2.** 2D-AFM images of STO films: STO, STO-N116, and STO-N516 (size- $2 \times 2 \mu\text{m}^2$ ). The inset shows 3D-AFM image of respective films.

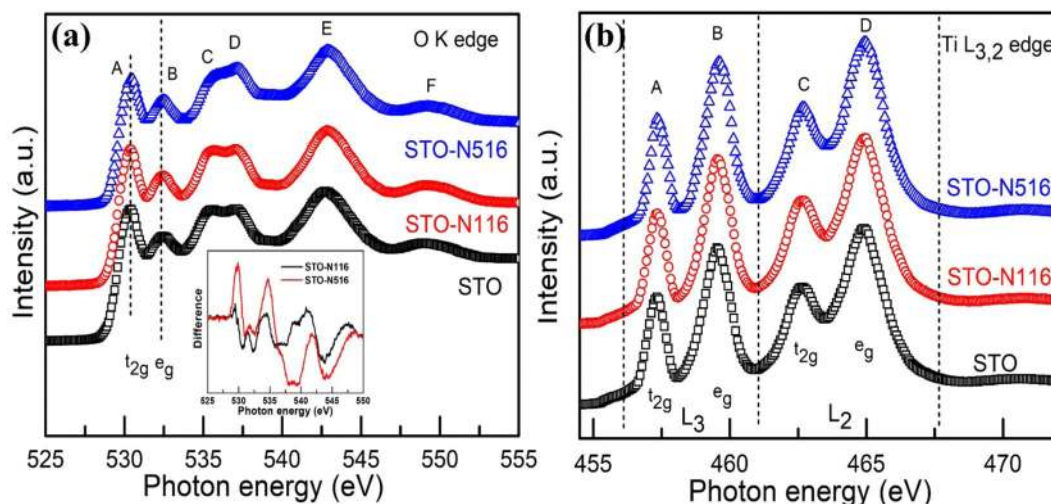


**Figure 3.** The X-ray absorption spectra of STO, STO-N116 and STO-N516 samples at (a) O K-edge and (b) Ti L-edge of STO, STO-N116 and STO-N516 samples. The Inset in Fig. 3(a) shows the difference spectra of O K-edge obtained by subtracting the implanted films from the STO spectrum.

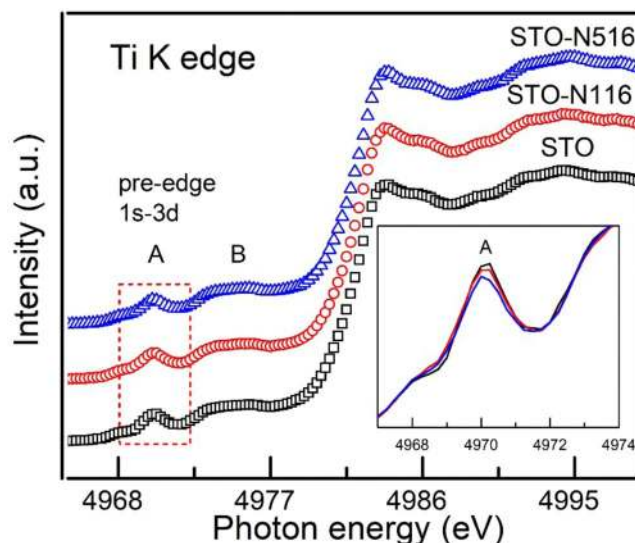
elements as a function of thickness and the ratio of elements Sr:Ti:O is found to be 1:1:2.4. However, this value is only indicative and not absolute as RBS is less sensitive to O element.

Figure 2 shows the AFM images of the STO pristine and N ion implanted thin films. The surface root mean square (RMS) roughness of the pristine film is small (0.94 nm) and after N ion implantation, there is an increase in surface roughness and decrease in grain size from 124 to 114 and 81 nm for STO-N116 and STO-N516 respectively.

Figure 3 show the X-ray absorption spectra at O K- and Ti L-edges corresponding the transitions from core level to unoccupied states following dipole selection rules. The O K-edge spectra of pristine and implanted films are shown in Fig. 3(a). The O K-edge features of STO are labelled as A, B, C, D, E and F. The first two main features, A and B, refer as  $t_{2g}$  and  $e_g$  states corresponding to the transitions from O 1s orbital to O  $2p_{\pi}$  and O  $2p_{\sigma}$  states hybridized with Ti 3d orbitals respectively. The features, C and D are assigned to the transitions from O 1s orbital to the unoccupied O 2p orbital hybridized with the Sr 4d, and E and F to the Sr 5sp and Ti 4sp orbitals respectively. The peak intensity in O K-edge is related to the number of unoccupied 2p orbitals and also reflects the hybridization with Ti 3d and Ti 4sp orbitals<sup>25</sup>. The crystal field splittings measured from the difference of  $t_{2g}$  and  $e_g$  is 2.06 eV for pristine which is smaller than the bulk value<sup>26</sup> and it decreases with the N implantation. This is attributed to the small Ti 3d-O 2p overlap resulting in small degree of hybridization<sup>26</sup>. In addition, the intensity ratio of  $t_{2g}$  to  $e_g$  changes with the ion implantation. For high N fluence, The  $t_{2g}/e_g$  ratio decreases as compared to the STO and STO-N516. Apart from this, there is a change in the relative intensities of C and D for STO-N516. Similar behaviour is observed by Mi *et al.*<sup>27</sup>. This change might be related to the distortion that occurs in the  $\text{TiO}_6$  octahedra in STO lattice<sup>28</sup>. Inset in Fig. 3(a) shows the difference spectra obtained by subtracting from the STO. From the difference spectra, it is evident that the STO has significant density of unoccupied states compared to STO-N116 and STO-N516. In other words, the density of unoccupied states in implanted samples decreases. This implies that by N ion implantation, the density of states increases.

The Ti L edge spectra of N implanted STO samples are shown in Fig. 3(b). The spectra at Ti  $L_{3,2}$  edges correspond to the transition from  $2p^6 3d^n$  to  $2p^5 3d^{n+1}$ . Here, in case of STO n is zero. Thus, Ti  $L_{3,2}$ -edges provide the





**Figure 4.** The spectra at Ti K edge of STO, STO-N116 and STO-N516. Inset shows the magnified view of pre-edge region assigned to 1s-3d transition.

direct information of the unoccupied 3d orbitals and sensitive to the local symmetry<sup>25,27</sup>. In this figure, the four spectral features, A, B, C and D, are assigned to the dipole transitions from Ti 2p<sub>3/2</sub> (L<sub>3</sub>) and 2p<sub>1/2</sub> (L<sub>2</sub>) orbitals split due to spin-orbit interaction to unoccupied 3d-orbitals, respectively. Out of these, features A & C correspond to t<sub>2g</sub> and B & D to e<sub>g</sub> orbitals<sup>27</sup>. In general, the spectral features of Ti L<sub>2</sub>-edge are very broad compared to Ti L<sub>3</sub>-edge. This is due to the much shorter lifetime of 2p<sub>1/2</sub> core holes via Coster–Kronig decay<sup>29</sup>. It is observed that there is noticeable broadening in the overall spectra of Ti L-edges which is attributed either to the nitrogen occupancy or defects introduced during N ion implantation. Further, the relative intensities of t<sub>2g</sub> and e<sub>g</sub> sub-bands are estimated from the fitting and it is observed that the ratio t<sub>2g</sub>/e<sub>g</sub> of L<sub>3</sub> orbital of STO-N116 and STO-N516 decreases as compared to the pristine sample. This indicates that there is local distortion and symmetry of Ti ions indicating change in the hybridization of Ti 3d and O 2p orbitals consistent with the O K-edge.

Figure 4 shows the X-ray absorption spectra at Ti K-edge of all the samples. The main peak in the spectrum at Ti K-edge corresponds to dipole allowed 1s to 4p transitions. The feature marked as A is known as pre-edge corresponds to 1s-3d quadrupole transition. The pre-edge region (see Inset of Fig. 4(b)) is the very sensitive to the displacement of Ti atom from its centro-symmetric position in TiO<sub>6</sub> octahedron<sup>30</sup>. The overall spectra of Ti K edges do not show any drastic change after N ion implantation. As observed in Fig. 4, the pre-edge peak intensity diminishes with the N implantation<sup>29</sup>. The reduction in pre-edge peak intensity is large for STO-N516 as compared to STO-N116 and the pristine films. These results are consistent with the Ti L- and O K-edge data.

To understand the electrical and thermoelectric properties, the temperature dependent resistivity and Seebeck co-efficient were measured. Figure 5 shows the resistivity of pristine and implanted films in the temperature range of 80–400 K. It is evident that the resistivity decreases with temperature indicating a typical semiconducting behaviour in all samples. For the film STO-N116, the resistivity increases as compared to the STO for the entire temperature range. At higher fluence, STO-N516, there is a significant reduction in resistivity compared to the pristine and STO-N116. This reduction is more visible, in particular, at low temperature.

Generally, for semiconductors, the band conduction governs the charge transport properties at high temperature<sup>31</sup>. In band conduction, charge carriers from localized states are thermally activated and transported to the delocalized states. However, in deformed or disordered materials at relatively low temperature, the charge carriers hop through localized states without excitation to the conduction band. Overall, there are mainly two types of conduction mechanisms in such materials, namely (a) band conduction or thermal activation process (b) hopping. This hopping mechanism can be further subdivided into two types: (i) nearest-neighbour-hopping (NNH) and (ii) variable-range-hopping (VRH) as shown in the schematic diagram, Fig. 6. The universal equation governing these conduction mechanisms in semiconductors is given by<sup>31</sup>

$$\rho(E) = \rho_o \exp \left[ \left( \frac{E_t}{k_B T} \right)^P \right] \quad (1)$$

where  $\rho_o$  is the resistivity coefficient,  $E_t$  is the transition energy,  $k_B$  is the Boltzmann constant and  $P$  ( $>0$ ) is the characteristic exponent. The exponent  $P$  defines a different kind of mechanism based upon the density of states at Fermi level<sup>31</sup>. For band conduction  $P = 1$ , and for variable range hopping  $P$  lies between 0 and 1<sup>32</sup>.

The experimental data are first analysed using the band conduction model where the exponent  $P = 1$  and  $E_t$  corresponds to thermal activation energy ( $E_a$ ) (Eq. (1)). It is observed that the resistivity data fits well linearly for the pristine film in the temperature range 333–410 K and for STO-N116 and STO-N516 from 285 to 410 K. This suggests that the existence of band conduction mechanism at high temperature regime. The thermal activation

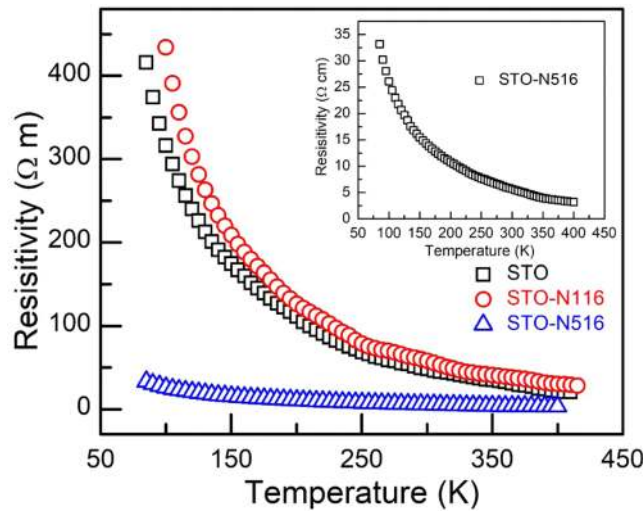


**Figure 5.** Temperature dependence of resistivity of pristine and N implanted STO thin films. All the films show semiconducting behaviour with temperature. Inset shows the resistivity of STO-N516 with temperature.

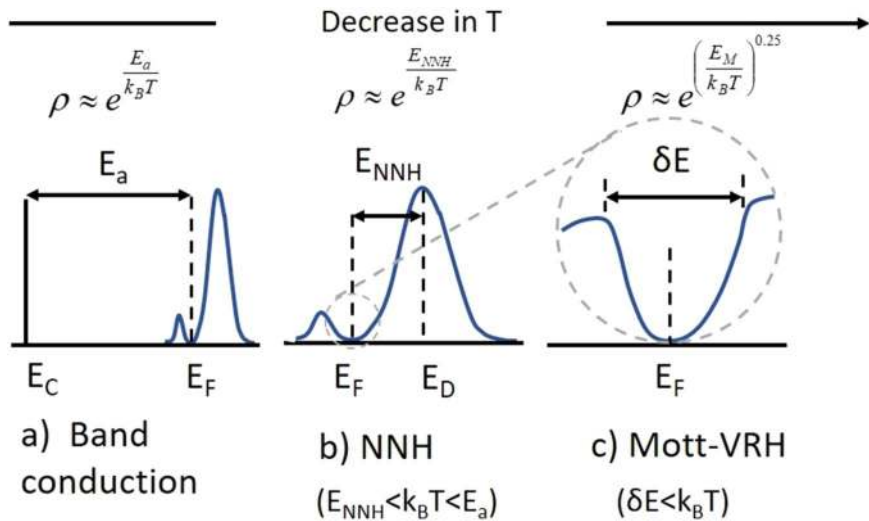


**Figure 6.** Schematics showing the conduction mechanisms as a function of temperature. (a) Band conduction, (b) NNH, and (c) VRH (Mott-type).

| Films    | $E_s$ (meV)<br>(300–400 K) | $E_a$ (meV)<br>(280–410 K) | $E_{NNH}$ (meV)<br>(160–300 K) | $E_M$ (meV)<br>(80–218 K) | $T_M$ (K)<br>(80–218 K) | $R_M/a$<br>( $K^{-0.25}$ ) | $E_a - E_s$<br>(meV) | $s$  |
|----------|----------------------------|----------------------------|--------------------------------|---------------------------|-------------------------|----------------------------|----------------------|------|
| STO      | 20                         | 100                        | 40                             | $0.43 T^{3/4}$            | 161928                  | $7.72/(T)^{1/4}$           | 101                  | 2.01 |
| STO-N116 | 32                         | 62                         | 32                             | $0.52 T^{3/4}$            | 360888                  | $9.19/(T)^{1/4}$           | 90                   | 1.67 |
| STO-N516 | 17                         | 59                         | 26                             | $0.38 T^{3/4}$            | 96388                   | $6.61/(T)^{1/4}$           | 78.32                | 2.66 |

**Table 1.** Transport parameters calculated in the temperature range (80–400 K).

energy ( $E_a$ ) required for the transportation of charge carriers to the delocalized states can be derived by a simple Arrhenius law and it is given in Table 1. Figure 7(a) shows the Arrhenius plot of  $\ln(\rho)$  vs.  $1/T$  and  $E_a$  is calculated from the slope. The thermal  $E_a$  for pristine STO is derived to be 100 meV which is comparable to the reported experimental results<sup>33</sup>. It is found that the  $E_a$  is found to decrease significantly after N ion implantation, i.e., in STO-N116 and STO-N516 as compared to the STO.

At relatively low temperature, the experimental data deviate from the Arrhenius law. This indicates that the conduction can no longer be described within the band conduction mechanism. The charge carriers do not have sufficient thermal energy to jump over the delocalized states and it is expected to conduct in the nearest localized states via hopping. In such cases, NNH may be the dominating transport mechanism wherein the exponent  $P$

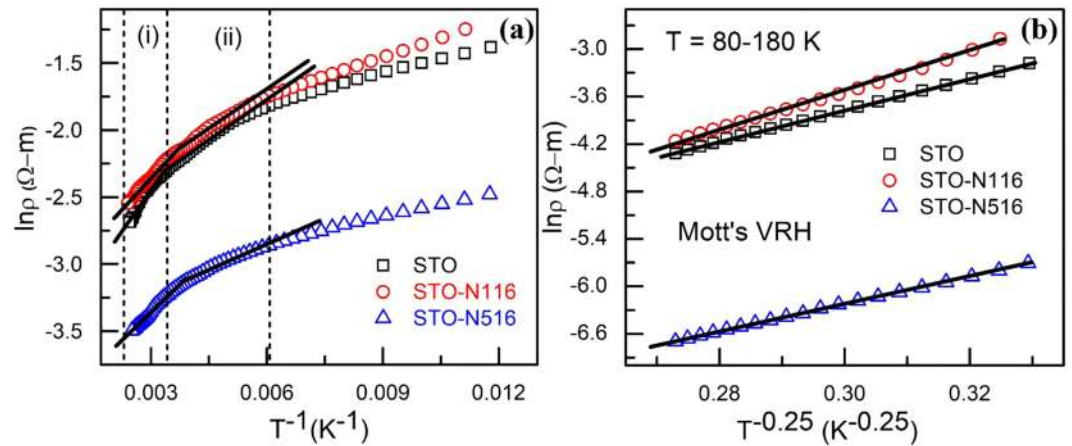


**Figure 7.** (a) plot of  $\ln \rho$  vs.  $1/T$  fitted using (i) band conduction model and (ii) NNH (180–300 K). The crossover temperature from band conduction to NNH is 333 K for STO and 285 K for STO-N116 and STO-N516. (b) Plot of  $\ln \rho$  vs.  $T^{-1/4}$  fitted using the VRH model. The solid black lines represent the regimes of the corresponding mechanisms.

still remains within 1 (see Eq. 1) and  $E_t$  represents as the nearest neighbour activation energy  $E_{NNH}$ . In NNH conduction mechanism, the charge carrier hop to the nearest neighbour sites but the activation energy required for hopping to empty sites is smaller than the  $E_a$ . The temperature dependence of resistivity in case of NNH is given below as<sup>31</sup>:

$$\rho(E) = \rho_{NNH} \exp\left(\frac{E_{NNH}}{k_B T}\right) \quad (2)$$

where  $\rho_{NNH}$  is a constant and  $E_{NNH}$  is the nearest neighbour activation energy.

As shown in Fig. 7(a), there exists a close relationship for NNH mechanism within temperature range 180–300 K. The NNH activation energy is calculated from the plot of  $\ln \rho$  vs.  $1/T$  and listed in Table 1. It is observed that  $E_{NNH}$  is found to be smaller than  $E_a$  for all the samples and hence suggests the presence of NNH conduction.

On further decrease in temperature ( $T < 180$  K), it is found that neither NNH nor band conduction model fits with the experimental data depicting that there is a crossover of conduction mechanism from the NNH to VRH. In lower temperature regime, the possibility of NNH reduces due to a small number of nearest neighbour empty sites which makes the charge carriers to hop between the localised states close to the Fermi level. In that case, the temperature dependence of resistivity can be better expressed by the Mott's VRH mechanism which is given as<sup>34</sup>

$$\rho = \rho_o \exp\left(\frac{T_M}{T}\right)^{\frac{1}{4}} \quad (3)$$

where  $T_M$  is the Mott's temperature and  $\rho_o$  is the resistivity coefficient. For the temperature, 84–218 K, the Mott's VRH conduction mechanism is used. The linear fit of  $\ln \rho$  against  $T^{-1/4}$  as shown in Fig. 7(b) implies that the Mott's VRH governs the transport in the low temperature regime. The characteristic Mott's temperature,  $T_M$ , obtained from the slope of the fitted curve and represented as<sup>34</sup>

$$T_M = \frac{18}{k_B a^3 N(E_F)} \quad (4)$$

where  $a$  is localization length and  $N(E_F)$  is the density of states at Fermi level. It is clear from this equation that  $T_M$  is inversely proportional to  $N(E_F)$ . At higher fluence of N ion implantation, STO-N516, the value of  $T_M$  decreases due to the enhancement of the  $N(E_F)$  at the Fermi level. Further, the ratio of average hopping ( $R_M$ ) distance to localization length ( $a$ ) can be calculated from the fitting parameters. According to Mott-VRH model, the average hopping distance ( $R_M$ ) must be larger than the localization length  $a$ , which is given as<sup>34</sup>

$$\frac{R_M}{a} = \frac{3}{8} \left(\frac{T_M}{T}\right)^{\frac{1}{4}} > 2 \quad (5)$$

The calculated values are listed in Table 1. From the fitting, the ratio,  $R_M/a$ , is found to be more than 2 for all samples in the temperature range (80–180 K). This is imperative that the Mott's VRH conduction mechanism is valid<sup>34</sup>.

In addition, the Mott hopping energy<sup>34</sup>,  $E_M$ , can be evaluated and listed in Table 1:

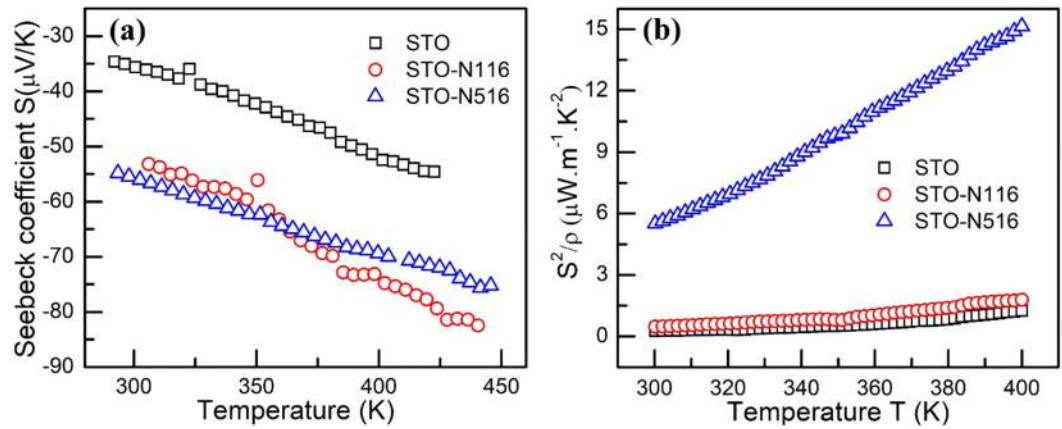


**Figure 8.** (a) Temperature dependence of the  $S$  of all the films, (b) Power factor as a function of temperature in range 300–400 K. The maximum power factor of  $15 \mu\text{Wm}^{-1} \text{K}^{-2}$  at 400 K for STO-N516.

$$E_M = \frac{1}{4} k_B T \left( \frac{T_M}{T} \right)^{\frac{1}{4}} \quad (6)$$

Above results show that with N ion implantation in STO, different conduction mechanisms are operative in the entire temperature range of 80–400 K. This suggests that at high temperature ( $T > 300$  K) and mid temperature range (180–300 K), the band conduction and NNH conduction mechanisms, respectively prevail and there is a crossover from NNH to Mott's VRH in low temperature regimes. These results are similar to that of other oxides like ZnO<sup>35</sup>. It may be noted that there exists no data related to STO in literature.

The Seebeck coefficient is measured in the temperature range of 300–400 K and displayed in Fig. 8(a). The sign of  $S$  is negative throughout the measured temperature range revealing  $n$ -type behaviour for all the samples and  $S$  increases with temperature. The room temperature value of  $S$  for pristine STO is  $35 \mu\text{V/K}$  which increases to  $52 \mu\text{V/K}$  and  $56 \mu\text{V/K}$  on N implantation with fluence  $1 \times 10^{16}$  and  $5 \times 10^{16}$  ion/cm<sup>2</sup>, respectively<sup>36</sup>. Fig. 8(b) shows the variation of power factor of N implanted thin films as a function of temperature. The STO-N516 film exhibits the highest power factor of  $15 \mu\text{Wm}^{-1} \text{K}^{-2}$  at 400 K and this enhancement is related to  $S$  and the electrical conductivity after N ion implantation.

The temperature dependence of  $S$  is represented by the Boltzmann's equation<sup>37</sup>,

$$S = - \frac{k}{e} \left( \frac{E_s}{k_B T} + A \right) \quad (7)$$

where  $E_s$  and  $A$  are represent as activation energy and scattering parameter for thermopower respectively. The linear dependence of  $S$  vs.  $1000/T$  is plotted and  $E_s$  is evaluated (see in Table 1). Here,  $E_s$  is represented as the energy difference between the Fermi level and bottom of the conduction band. The derived  $E_s$  is compared with  $E_a$  from the resistivity data in the same temperature range (330–400 K) and found to be smaller than  $E_a$ . Using the activation energy determined from the resistivity and thermopower data, one can understand the existence of the localised levels in the band gap and hence successive conduction mechanisms. The concept of large  $E_a$  over  $E_s$  lies in such a way that in the resistivity measurements, the current flows through the film in a closed loop because the charge carriers need to overcome the highest potential barrier during the conduction. However, in thermopower, it is an open circuit measurements wherein the charge carriers have to cross only the local fluctuations<sup>10,38</sup>. The difference  $\Delta E$  quantifies the magnitude of potential fluctuations. In the present case, the difference is positive suggesting that the thermal activation process governs the conduction in high temperature regime. These observations also support the resistivity data discussed above for the same temperature range of 300–410 K. The difference in the activation energies between both measurements can also be expressed as a dimensionless quantity  $Q$  given by<sup>39</sup>

$$Q = \ln \sigma - \frac{eS}{k} = C - \frac{\Delta E}{kT} \quad (8)$$

The value of  $\Delta E$  is estimated from the slope by a linear fit of  $Q$  vs  $1000/T$  and found in accordance with the calculated difference  $E_a - E_s$ .

For the detailed understanding of carrier transport, another approach of dispersive transport mechanism can be considered<sup>40</sup>. The dispersive transport is typically associated with conduction through delocalized band states (band conduction). In this model, thermopower–conductivity relation obtained from the Sommerfeld expansion allows one to identify the scattering mechanism by estimating the value of exponent  $s$  in the following equation<sup>40</sup>.



$$S = \frac{k_B \pi^2}{q} \frac{1}{3} s \left( \frac{\sigma}{\sigma_{E_0}} \right)^{-1/s} \quad (9)$$

where  $S$ ,  $\sigma$ ,  $\sigma_{E_0}$ , and  $s$  are Seebeck coefficient, conductivity, transport coefficient in the units of conductivity and transport exponent, respectively. The plot of  $\ln S$  vs.  $\ln \sigma$  is employed to extract  $s$  from the slope. The value of  $s$  can be ascribed to different scattering mechanisms, (a) polar-optical phonon scattering ( $s = 2$ ) (b) ionized impurity scattering ( $s = 3$ ) and (c) point defect scattering ( $s = 1$ )<sup>40</sup>. The calculated value of  $s$  for pristine STO is 2 which corresponds to polar-optical phonon scattering. For STO-N116 and STO-N516,  $s$  is 1.67 and 2.66 respectively which suggest that scattering mechanism is changing with the implantation from optical phonon scattering to ionized impurity scattering. The value of  $s$  for each sample is listed in Table 1.

The ion implantation is a technique that offers precise control of implanted ion/dopant species, profile and temperature. This process involves interaction with materials displacing the host atoms from their original sites and transferring energy to electrons causing ionization and excitations<sup>41</sup>. It can be used to introduce impurities, defects such as oxygen vacancies into lattice, or to investigate the novel properties resulting from the impurity-defect interactions<sup>12,42</sup>. Oxygen deficiency can have a positive effect on the thermoelectric properties. Kumar *et al.* have demonstrated that an increase in concentration of oxygen vacancies enhance simultaneously the carrier concentration and Seebeck coefficient. This results in a large power factor<sup>43</sup>. The main advantages of introducing oxygen vacancies via low-energy ion bombardment over vacuum annealing are (i) the distribution of vacancies can be spatially localized as it is dependent on the penetration depth of the implanted ions and (ii) the absence of secondary phases that occurs during high temperature vacuum annealing leading to distortion of the STO lattice<sup>44</sup>. In the present study, the 60 keV N ion implantation leads to amorphization of few surface layers of STO thin films. Using SRIM software, the nuclear energy loss ( $S_n$ ) and electronic energy loss ( $S_e$ ) are found to be 11.8 eV/Å and 33 eV/Å respectively. The relative contribution of both these mechanisms induces lattice defects and dislocations causing amorphization as evidenced from the XRD. The post annealing helps in the incorporation of N ions in STO lattice either at interstitial or substitutional sites<sup>27</sup> and also displaces the atoms to reduce the radiation damage caused by implantation<sup>45</sup>. This leads to stronger crystalline nature. Similar observation has been reported by Kumar *et al.* in case of N ion implanted CeO<sub>2</sub><sup>46</sup>. The X-ray absorption measurements performed to probe the local electronic structure that shows the change in Ti 3d-O2p hybridization and local symmetry resulting from the defects generated by ion implantation. This leads to change in parameters such as crystal field splittings and the  $t_{2g}/e_g$  ratio. This might be attributed to the decrease of transition probability to the empty 3d orbitals due to the reduction in unoccupied orbitals with N occupancy or the defects mainly oxygen vacancy created during implantation. Another reason could be the distortion of TiO<sub>6</sub> octahedra in STO that modifies the Ti 3d and O 2p hybridization. Hence, this behaviour contributes to the increased conductivity of STO-N516 sample. However, the crystal structure is retained. The AFM images confirm that there is a decrease in the grain size of the films after implantation. Implantation creates defects and vacancies in the lattice, which leads to the increase in the grain boundaries and these in turn scatter the phonons. The films of STO-N516 exhibits large grain boundaries and such increase causes potential barrier scattering resulting in the enhancement of Seebeck coefficient<sup>47</sup>. In addition to this, decrease in crystal size serves as the scattering center of the phonons and hence enhances the Seebeck coefficient and thermal conductivity. This implies that one needs to optimize the crystallite size and oxygen vacancies that control the conductivity and hence achieve maximum ZT.

In the high temperature range, the temperature dependence of resistivity can be explained by band conduction mechanism where the charge carriers have sufficient energy to jump across conduction band. The activation energy calculated from the Arrhenius plot decreases with ion implantation. This may arise due to additional localized states in the band gap. In the mid temperature range, the charge carriers hop to the nearest sites and lowers the activation energy compared to thermal activation energy. As the temperature decreases, the resistivity data deviate from the linear regression of band conduction and NNH mechanisms, and leads to the Mott's VRH mechanism<sup>34</sup>. At lower temperature, due to insufficient thermal energy, the charge carriers can hop across the localised empty sites at larger distances. The characteristic Mott temperature,  $T_M$  is found to be lowest for high fluence. This results in an enhanced density of states at the Fermi level which is responsible for the increased conductivity. For a better understanding of transport phenomenon,  $S$  is also analysed by calculating various parameters. The activation energy  $E_s$  evaluated from the Boltzmann's equation is found to be smaller than the thermal activation energy  $E_a$  and positive  $\Delta E = E_a - E_s$  suggests the presence of potential fluctuation caused by ion defects. It is found that ion implantation changes the scattering mechanism from optical phonons to defect assisted scattering for STO-N116 sample resulting in a decreased value of  $s$  (1.67). On further implantation, i.e., STO-N516, doped impurities are sufficiently large in number to contribute and modify the scattering mechanisms which result in ionized impurity scattering with a large value of  $s$  (2.66). In the present case, the observed scattering centres and localized states in the band gap after implantation might originate from: (a) the defects and distortion in the STO lattice, (b) the oxygen vacancies, and (c) the modification of band structure due to N doping. In other words, the materials having high impurity scattering centres are likely to provide enhanced  $S$  and power factor. However, a detailed investigation using different ion beams with different oxygen stoichiometry is required to understand the exact common transport and scattering mechanisms and their tunabilities in these materials.

There are a few studies on the first principles calculations using the Density functional theory (DFT) for N doped SrTiO<sub>3</sub>, and TiO<sub>2</sub> systems assuming the incorporation of N ions such as substitutional, interstitial and oxygen vacancies. The results from Mi *et al.* and Valentin *et al.* reported that the N 2p impurity states are localized and lie slightly above the top of the O 2p valence band<sup>27,48</sup>. They also reported that there is no shift in the position of the O 2p valence band, as well as of the conduction band, with respect to the pristine material. These result in electrons getting trapped easily in the high-energy levels when excited into the conduction band, and responsible



for the increased electrical conductivity. On the other hand, Rumaiz *et al.* proposes a bandgap narrowing due to the hybridization of Ti 3d states with unoccupied both O 2p states and N 2p states<sup>49</sup>. The valence-band structure exhibits tailing to lower binding energies due to the incorporation of less tightly bound N 2p level that is hybridized with O 2p level causing a reduction in bandgap.

These first principal calculations can be easily compared with the experimental XAS data. The spectral features of the XAS represent the density of unoccupied states. This is theoretically comparable with band structure calculations that provide projected density of states (DOS)<sup>28</sup>. Inset in Fig. 3(a) shows the difference spectra obtained by subtracting from the STO. From the difference spectra, it is evident that the STO has significant density of unoccupied states compared to STO-N116 and STO-N516. In other words, the density of unoccupied states in implanted samples decreases. This implies that by N ion implantation, the density of states increases. Hence, this increase in DOS is responsible for enhanced power factor.

To conclude, N ion implantation creates defects and vacancies, which affect the transport properties of the carriers. It modifies the transport mechanism by creating trap centers and defects which act as scattering centers<sup>10</sup>. The defects induced leads to the reduction of thermal conductivity and have less effect on S, which in turn improves the ZT value. These observed increase in S could be accounted from the modification of these properties under implantation suggesting scattering of phonons by ionized impurity and vacancies formed in the sample.

## Methods

The STO films ( $5 \times 10 \text{ mm}^2$ ) were fabricated by pulsed laser deposition (PLD) system (Excel Instruments, Mumbai) using a KrF excimer laser (248 nm wavelength, 10 Hz repetition rate and 20 ns pulse duration) in Ar atmosphere at a substrate temperature of 700 °C. The p-type Si substrate was used for deposition. Before PLD deposition, only RCA-1 cleaning of substrate was performed and no etching in HF was done to protect the native SiO<sub>2</sub> layer present on Si substrate<sup>50</sup>. This was confirmed by performing I-V on bare substrates. The STO films were grown by ablation of STO bulk ceramic target at an energy density of 4.2 J/cm<sup>2</sup> and the target was rotated to ensure uniform deposition. To clean the surface, pre-ablation was done using 500 shots on the target surface. The STO layer was deposited over the insulating SiO<sub>2</sub> layer. The resistance of the STO films is in kΩ which excludes any contribution from the substrate. This implies that there is no effect from the substrate. The thickness of all films was measured as ~260 nm using Surface Profilometer (Ambios, XP-200, USA). The X-ray diffraction pattern of these STO films exhibit crystalline nature. These films were then implanted with 60 keV N<sup>+</sup> ion beam with two different fluences,  $1 \times 10^{16}$  and  $5 \times 10^{16}$  ion/cm<sup>2</sup> using Low Energy Ion Beam Facility (LEIBF) at Inter University Accelerator Centre (IUAC), New Delhi. The energy of ions is selected to implant N ions within STO layer of thickness 260 nm. The projected range of N ions in STO lattice has been pre-simulated using TRIM (Transport of Ions in Matter) code and is estimated to be ~102 nm ( $\pm 40$  nm, straggling)<sup>51</sup>. Post implantation vacuum annealing was performed at 700 °C for 2 h. For simplicity, hereafter, annealed films of pristine,  $1 \times 10^{16}$  ions/cm<sup>2</sup> and  $5 \times 10^{16}$  ions/cm<sup>2</sup> referred as STO, STO-N116, and STO-N516, respectively. The equivalent doping concentrations in STO lattice are estimated to be  $3.3 \times 10^{20}$  ions/cm<sup>3</sup> and  $1.5 \times 10^{21}$  ions/cm<sup>3</sup> for STO-N116 and STO-N516 respectively.

The X-ray diffraction (XRD) measurements were performed to determine the structural information at glancing angle (1°) by Philips X'pert PRO (Model PW 3040) diffractometer in the range of 20°–80°. For compositional and thickness measurements, Rutherford backscattering (RBS) spectrometry was performed using 2 MeV H<sup>+</sup> ions at IUAC, New Delhi. The scattering angle was maintained at 165°. The surface morphology was examined by Multi Mode Scanning Probe Microscopy (Bruker) in tapping mode. In order to investigate the chemical and electronic structural information, Ti L- and O K-edge spectra were recorded in total electron yield (TEY) mode at high-energy spherical grating monochromator (HSGM) beamline 20A1 of the National Synchrotron Radiation Research Centre (NSRRC) in Hsinchu, Taiwan. The energy resolution  $\Delta E/E$  was of order of 1/5000. The Ti K edge measurements were performed at wiggler beamline 17C in total fluorescence yield (TFY) and Ti foil was used for calibration. The photon energy resolution is 0.3 eV. The S and resistivity measurements were performed using an in-house developed experimental set-up<sup>52</sup>.

## Conclusion

In summary, ion implantation studies on PLD deposited STO thin films were carried out to understand the electrical transport and scattering mechanisms. The XRD confirms the cubic perovskite phase of pristine and implanted films. The X-ray absorption spectra show that N implantation affects the local symmetry of TiO<sub>6</sub> octahedron by generating defects mainly oxygen vacancies. There is an enhancement in electrical conductivity and thermopower at high implantation dose. The electrical transport properties of N ion implanted STO films reveal different conduction mechanisms: the band conduction in the high temperature regime, nearest neighbour and variable range hopping in the low temperature regime attributed to the presence of defect induced localized states in the band gap. The increased power factor ( $15 \mu\text{Wm}^{-1} \text{K}^{-2}$ ) for higher fluence film depicts the significance of ion implantation technique which provides a new tool for defect engineering in the applications of thermoelectric devices.

## References

1. Zhao, D. & Tan, G. A review of thermoelectric cooling: Materials, modeling and applications. *Applied Thermal Engineering* **66**, 15–24, <https://doi.org/10.1016/j.applthermaleng.2014.01.074> (2014).
2. Alam, H. & Ramakrishna, S. A review on the enhancement of figure of merit from bulk to nano-thermoelectric materials. *Nano Energy* **2**, 190–212, <https://doi.org/10.1016/j.nanoen.2012.10.005> (2013).
3. Snyder, G. J. & Toberer, E. S. Complex thermoelectric materials. *Nature Materials* **7**, 105, <https://doi.org/10.1038/nmat2090> (2008).
4. He, J., Liu, Y. & Funahashi, R. Oxide thermoelectrics: The challenges, progress, and outlook. *Journal of Materials Research* **26**, 1762–1772, <https://doi.org/10.1557/jmr.2011.108> (2011).

5. Kaurav, N., Wu, K. K., Kuo, Y. K., Shu, G. J. & Chou, F. C. Seebeck coefficient of  $\text{Na}_x\text{CoO}_2$ : Measurements and a narrow-band model. *Physical Review B* **79**, <https://doi.org/10.1103/PhysRevB.79.075105> (2009).
6. Wang, H., Su, W., Liu, J. & Wang, C. Recent development of n-type perovskite thermoelectrics. *Journal of Materiomics* **2**, 225–236, <https://doi.org/10.1016/j.jmat.2016.06.005> (2016).
7. Ouyang, Y., Zhang, Z., Li, D., Chen, J. & Zhang, G. Emerging Theory, Materials, and Screening Methods: New Opportunities for Promoting Thermoelectric Performance. *Annalen der Physik*, 1800437, <https://doi.org/10.1002/andp.201800437> (2019).
8. Zhang, X. & Zhao, L.-D. Thermoelectric materials: Energy conversion between heat and electricity. *Journal of Materiomics* **1**, 92–105, <https://doi.org/10.1016/j.jmat.2015.01.001> (2015).
9. Bala, M. *et al.* Enhancement of thermoelectric power of PbTe thin films by Ag ion implantation. *Journal of Applied Physics* **121**, 215301, <https://doi.org/10.1063/1.4984050> (2017).
10. Kumar, A. *et al.* Enhancement of thermopower in GaN by ion irradiation and possible mechanisms. *Applied Physics Letters* **111**, 222102, <https://doi.org/10.1063/1.4996410> (2017).
11. Alaie, S. *et al.* Reduction and Increase in Thermal Conductivity of Si Irradiated with Ga(+) via Focused Ion Beam. *ACS applied materials & interfaces* **10**, 37679–37684, <https://doi.org/10.1021/acsami.8b11949> (2018).
12. Kan, D. *et al.* Blue-light emission at room temperature from Ar<sup>+</sup>-irradiated SrTiO<sub>3</sub>. *Nature Materials* **4**, 816–819, <https://doi.org/10.1038/nmat1498> (2005).
13. Koumoto, K., Wang, Y., Zhang, R., Kosuga, A. & Funahashi, R. Oxide Thermoelectric Materials: A Nanostructuring Approach. *Annual Review of Materials Research* **40**, 363–394, <https://doi.org/10.1146/annurev-matsci-070909-104521> (2010).
14. Lee, H. N., Ambrose Seo, S. S., Choi, W. S. & Rouleau, C. M. Growth control of oxygen stoichiometry in homoepitaxial SrTiO<sub>3</sub> films by pulsed laser epitaxy in high vacuum. *Scientific reports* **6**, 19941, <https://doi.org/10.1038/srep19941> (2016).
15. Son, J. *et al.* Epitaxial SrTiO<sub>3</sub> films with electron mobilities exceeding 30,000 cm<sup>2</sup> V<sup>-1</sup> s<sup>-1</sup>. *Nature Materials* **9**, 482, <https://doi.org/10.1038/nmat2750> (2010).
16. Ohta, S. *et al.* Large thermoelectric performance of heavily Nb-doped SrTiO<sub>3</sub> epitaxial film at high temperature. *Applied Physics Letters* **87**, 092108, <https://doi.org/10.1063/1.2035889> (2005).
17. Wang, N. *et al.* Enhanced thermoelectric performance of Nb-doped SrTiO<sub>3</sub> by nano-inclusion with low thermal conductivity. *Scientific reports* **3**, 3449, <https://doi.org/10.1038/srep03449> (2013).
18. Zhang, Y. *et al.* Double thermoelectric power factor of a 2D electron system. *Nature Communications* **9**, 2224, <https://doi.org/10.1038/s41467-018-04660-4> (2018).
19. Ohta, H. *et al.* Giant thermoelectric Seebeck coefficient of a two-dimensional electron gas in SrTiO<sub>3</sub>. *Nat Mater* **6**, 129–134, <https://doi.org/10.1038/nmat1821> (2007).
20. Mune, Y., Ohta, H., Koumoto, K., Mizoguchi, T. & Ikuhara, Y. Enhanced Seebeck coefficient of quantum-confined electrons in SrTiO<sub>3</sub>/SrTiO<sub>3</sub>.8Nb<sub>0.2</sub>O<sub>3</sub> superlattices. *Applied Physics Letters* **91**, 192105, <https://doi.org/10.1063/1.2809364> (2007).
21. Liu, C. M., Zu, X. T. & Zhou, W. L. Photoluminescence of nitrogen doped SrTiO<sub>3</sub>. *Journal of Physics D: Applied Physics* **40**, 7318–7322, <https://doi.org/10.1088/0022-3727/40/23/011> (2007).
22. Janotti, A., Jalan, B., Stemmer, S. & Walle, C. G. V. D. Effects of doping on the lattice parameter of SrTiO<sub>3</sub>. *Applied Physics Letters* **100**, 262104, <https://doi.org/10.1063/1.4730998> (2012).
23. Kajimoto, R. *et al.* Elastic and dynamical structural properties of La and Mn-doped SrTiO<sub>3</sub> studied by neutron scattering and their relation with thermal conductivities. *Scientific reports* **8**, 9651, <https://doi.org/10.1038/s41598-018-27984-z> (2018).
24. Doolittle, L. R. Algorithms for the rapid simulation of Rutherford backscattering spectra. *Nuclear Instruments and Methods in Physics Research Section B: Beam Interactions with Materials and Atoms* **9**, 344–351, [https://doi.org/10.1016/0168-583X\(85\)90762-1](https://doi.org/10.1016/0168-583X(85)90762-1) (1985).
25. Soriano, L., Abbate, M., Fernández, A., González-Elipe, A. R. & Sanz, J. M. Chemical Analysis of Ternary Ti Oxides using Soft X-ray Absorption Spectroscopy. *Surface and Interface Analysis* **25**, 804–808, [https://doi.org/10.1002/\(sici\)1096-9918\(199709\)25:10<804::aid-sia303>3.0.co;2-3](https://doi.org/10.1002/(sici)1096-9918(199709)25:10<804::aid-sia303>3.0.co;2-3) (1997).
26. de Groot, F. M. F. *et al.* Oxygen 1s-x-ray absorption of tetravalent titanium oxides: A comparison with single-particle calculations. *Physical Review B* **48**, 2074–2080, <https://doi.org/10.1103/PhysRevB.48.2074> (1993).
27. Mi, Y. Y. *et al.* Thermal stability of nitrogen-doped SrTiO<sub>3</sub> films: Electronic and optical properties studies. *Journal of Applied Physics* **101**, 063708, <https://doi.org/10.1063/1.2713350> (2007).
28. Asokan, K. *et al.* Electronic structures of Ba<sub>1-x</sub>CaxTiO<sub>3</sub> studied by x-ray absorption spectroscopy and theoretical calculation. *Journal of Physics: Condensed Matter* **13**, 11087–11095, <https://doi.org/10.1088/0953-8984/13/48/332> (2001).
29. Ra, W., Nakayama, M., Cho, W., Wakihara, M. & Uchimoto, Y. Electronic and local structural changes in Li(2 + x)Ti<sub>3</sub>O<sub>7</sub> ramsdellite compounds upon electrochemical Li-ion insertion reactions by X-ray absorption spectroscopy. *Physical chemistry chemical physics: PCCP* **8**, 882–889, <https://doi.org/10.1039/b512740h> (2006).
30. Frenkel, A. I. *et al.* Origin of polarity in amorphous SrTiO<sub>3</sub>. *Physical review letters* **99**, 215502, <https://doi.org/10.1103/PhysRevLett.99.215502> (2007).
31. Bougiatioti, P. *et al.* Electrical transport and optical band gap of NiFe<sub>2</sub>O<sub>4</sub> thin films. *Journal of Applied Physics* **122**, 225101, <https://doi.org/10.1063/1.4999428> (2017).
32. González, J. C. *et al.* Hopping conduction and persistent photoconductivity in Cu<sub>2</sub>ZnSnS<sub>4</sub> thin films. *Journal of Physics D: Applied Physics* **46**, 155107, <https://doi.org/10.1088/0022-3727/46/15/155107> (2013).
33. Drożdż, E. & Koleżyński, A. The structure, electrical properties and chemical stability of porous Nb-doped SrTiO<sub>3</sub> – experimental and theoretical studies. *RSC Advances* **7**, 28898–28908, <https://doi.org/10.1039/c7ra04205a> (2017).
34. Lu, C. *et al.* Crossover of conduction mechanism in Sr<sub>2</sub>IrO<sub>4</sub> epitaxial thin films. *Applied Physics Letters* **105**, 082407, <https://doi.org/10.1063/1.4894465> (2014).
35. Huang, Y.-L., Chiu, S.-P., Zhu, Z.-X., Li, Z.-Q. & Lin, J.-J. Variable-range-hopping conduction processes in oxygen deficient polycrystalline ZnO films. *Journal of Applied Physics* **107**, 063715, <https://doi.org/10.1063/1.3357376> (2010).
36. Kumar, S. R., Barasheed, A. Z. & Alshareef, H. N. High temperature thermoelectric properties of strontium titanate thin films with oxygen vacancy and niobium doping. *ACS applied materials & interfaces* **5**, 7268–7273, <https://doi.org/10.1021/am4015956> (2013).
37. Shirai, K. & Yamanaka, K. Mechanism behind the high thermoelectric power factor of SrTiO<sub>3</sub> by calculating the transport coefficients. *Journal of Applied Physics* **113**, 053705, <https://doi.org/10.1063/1.4788809> (2013).
38. Dyalasingh, H. M. & Kakalios, J. Thermopower and conductivity activation energies in hydrogenated amorphous silicon. *Physical Review B* **54**, 7630–7633, <https://doi.org/10.1103/PhysRevB.54.7630> (1996).
39. Brandt, M. S., Herbst, P., Angerer, H., Ambacher, O. & Stutzmann, M. Thermopower investigation of n- and p-type GaN. *Physical Review B* **58**, 7786–7791, <https://doi.org/10.1103/PhysRevB.58.7786> (1998).
40. Kang, S. D., Dylla, M. & Snyder, G. J. Thermopower-conductivity relation for distinguishing transport mechanisms: Polaron hopping in CeO<sub>2</sub> and band conduction in SrTiO<sub>3</sub>. *Physical Review B* **97**, <https://doi.org/10.1103/PhysRevB.97.235201> (2018).
41. Avasthi, D. K. & Mehta, G. K. *Swift heavy ions for materials engineering and nanostructuring*. Vol. 145 (Springer Science & Business Media, 2011).
42. Kato, Y., Shimada, T., Shiraki, Y. & F. Komatsubara, K. Electrical conductivity of disordered layers in GaAs crystal produced by ion implantation. *Journal of Applied Physics* **45**, 1044–1049, <https://doi.org/10.1063/1.1663366> (1974).

43. Kumar, S. R. S., Abutaha, A. I., Hedhili, M. N. & Alshareef, H. N. Effect of oxygen vacancy distribution on the thermoelectric properties of La-doped SrTiO<sub>3</sub> epitaxial thin films. *Journal of Applied Physics* **112**, 114104, <https://doi.org/10.1063/1.4767840> (2012).
44. Potzger, K. *et al.* Defect-induced ferromagnetism in crystalline SrTiO<sub>3</sub>. *Journal of Magnetism and Magnetic Materials* **323**, 1551–1562, <https://doi.org/10.1016/j.jmmm.2011.01.018> (2011).
45. Rankin, J., McCallum, J. & Boatner, L. The effect of annealing environments on the epitaxial recrystallization of ion-beam-amorphized SrTiO<sub>3</sub>. *Journal of Materials Research* **7**, 717–724 (1992).
46. Kumar, P. *et al.* Structural, optical and magnetic properties of N ion implanted CeO<sub>2</sub> thin films. *RSC Advances* **7**, 9160–9168 (2017).
47. Bala, M. *et al.* Enhancement of thermoelectric power of PbTe:Ag nanocomposite thin films. *RSC Advances* **5**, 25887–25895, <https://doi.org/10.1039/c5ra01000d> (2015).
48. Di Valentin, C., Pacchioni, G. & Selloni, A. Origin of the different photoactivity of N-doped anatase and rutile TiO<sub>2</sub>. *Physical Review B* **70**, 085116 (2004).
49. Rumaiz, A. K. *et al.* Oxygen vacancies in N doped anatase TiO<sub>2</sub>: Experiment and first-principles calculations. *Applied Physics Letters* **95**, 262111, <https://doi.org/10.1063/1.3272272> (2009).
50. Wang, S. J., Ong, C. K., You, L. P. & Xu, S. Y. Epitaxial growth of yttria-stabilized zirconia oxide thin film on natively oxidized silicon wafer without an amorphous layer. *Semiconductor Science and Technology* **15**, 836–839, <https://doi.org/10.1088/0268-1242/15/8/309> (2000).
51. Ziegler, J. F., Ziegler, M. D. & Biersack, J. P. SRIM – The stopping and range of ions in matter (2010). *Nuclear Instruments and Methods in Physics Research Section B: Beam Interactions with Materials and Atoms* **268**, 1818–1823, <https://doi.org/10.1016/j.nimb.2010.02.091> (2010).
52. Tripathi, T. S., Bala, M. & Asokan, K. An experimental setup for the simultaneous measurement of thermoelectric power of two samples from 77 K to 500 K. *The Review of scientific instruments* **85**, 085115, <https://doi.org/10.1063/1.4891631> (2014).

## Acknowledgements

One of the authors (AB) is grateful to the CSIR for providing SRF fellowship. The authors would like to thank Mr. Kedar Mal and Sunil Ojha for their help in ion implantation using LEIBF and RBS facility of IUAC. The authors are also thankful to NSRRC, Taiwan for XAS measurements and MRC, MNIT Jaipur for AFM measurements. The authors (KA and AM) would like to thank Indo-Taiwan bilateral (project no: GITA/DTS/TWN/P-64/2015) under GITA-Department of Science and Technology for providing financial support including research fellowship. Author (CLD) thanks MoST for the projects: AS-iMATE-108-23, MoST 108-2218-E-032-003-MY3, MoST 107-2112-M-032-004-MY3 and MoE for Taiwan Experience Education Program (TEEP).

## Author Contributions

A.B. is the Ph.D student who carried out the research work, analysed the data and wrote the manuscript with the help of her thesis advisor K. Asokan. A.M. and M.B. helped in measurement and analysis of electrical and thermoelectric characterization. D.H. and T.S. helped in deposition of the samples and A.F.M. characterization. C.L.D. and C.L.C. performed the XAS measurements. A.K. and R.M. contributed in the data analysis and writing part.

## Additional Information

**Supplementary information** accompanies this paper at <https://doi.org/10.1038/s41598-019-51079-y>.

**Competing Interests:** The authors declare no competing interests.

**Publisher's note** Springer Nature remains neutral with regard to jurisdictional claims in published maps and institutional affiliations.



**Open Access** This article is licensed under a Creative Commons Attribution 4.0 International License, which permits use, sharing, adaptation, distribution and reproduction in any medium or format, as long as you give appropriate credit to the original author(s) and the source, provide a link to the Creative Commons license, and indicate if changes were made. The images or other third party material in this article are included in the article's Creative Commons license, unless indicated otherwise in a credit line to the material. If material is not included in the article's Creative Commons license and your intended use is not permitted by statutory regulation or exceeds the permitted use, you will need to obtain permission directly from the copyright holder. To view a copy of this license, visit <http://creativecommons.org/licenses/by/4.0/>.

© The Author(s) 2019